

Structure Analysis of Exfoliated Unilamellar Crystallites of Manganese Oxide Nanosheets

Katsutoshi Fukuda,^{†,‡} Izumi Nakai,^{*,‡} Yasuo Ebina,[†] Masahiko Tanaka,[†] Takeharu Mori,[§] and Takayoshi Sasaki^{*,†}

Nanoscale Materials Center, National Institute for Materials Science, 1-1 Namiki, Tsukuba, Ibaraki 305-0044, Japan, Department of Applied Chemistry, Tokyo University of Science, 1-3 Kagurazaka, Shinjuku, Tokyo 162-8601, Japan, and Photon Factory, Institute of Materials Structure Science, High Energy Accelerator Research Organization, 1-1 Oho, Tsukuba, Ibaraki 305-0801, Japan

Received: March 7, 2006; In Final Form: June 23, 2006

Structure analysis of unilamellar manganese oxide nanosheets obtained via exfoliation of layered manganese oxides was carried out utilizing synchrotron radiation (SR) X-ray in-plane diffraction and polarization-dependent total reflection fluorescence X-ray absorption fine structure (PTRF-XAFS) analyses. A combination of SR excitation and the total reflection of incoming X-rays provides signals strong enough for both analyses even from a monolayer of the MnO₂ nanosheets having a concentration of 0.7 $\mu\text{g cm}^{-2}$. In addition, the mean oxidation state of constituent manganese ions in the MnO₂ sheets was estimated on the basis of XANES spectra, and bond valence sum calculations with the bond length obtained from the present EXAFS analyses. The obtained structural data revealed that the two-dimensional lattice of the MnO₂ sheets underwent a slight elongation upon delamination. These changes correspond to approximately 1% expansion of sheet area and 1–2% expansion of thickness, which can be understood by reduction of the mean oxidation number of manganese ions in the sheet through the exfoliation process.

Introduction

Unilamellar nanosheet crystallites obtained via delamination of layered compounds such as clay minerals,^{1,2} sulfides,^{3,4} and oxides^{5–7} are a unique class of nanomaterials that exhibit interesting physical and chemical properties associated with the size and shape in the nanometer-scale range. In particular, manganese oxide nanosheets,^{7,8} the precursor of which is a layered ternary oxide with the chemical composition of A_xMnO₂, where A represents alkali metal ions (see Figure 1), undergo exfoliation into single host layers through soft-chemical procedures. They are attractive functional materials as a new family of manganese oxides, which have a wide range of applications, e.g., cathode materials for Li secondary batteries,⁹ porous materials for catalysts,¹⁰ and magnetic materials with colossal magnetoresistance.¹¹ The nanosheet crystallites possess a number of interesting features; they have a thickness below 10 Å and a lateral size from submicrometers to micrometers. The high anisotropy is greatly different from that of other nanomaterials, which are usually spherical or rodlike in shape. Not only their redoxable capability arising from Mn³⁺/Mn⁴⁺ chemical conversion¹² but also their semiconducting property peculiar to the nanoscopic state of the nanosheet crystallites¹³ may pave the way for new applications for the manganese oxides. In addition, a recently developed layer-by-layer self-assembly technique and flocculation methods will be useful to create a variety of novel nanostructured materials by using the nanosheets as an inorganic building block.^{14,15}

Structure analysis of exfoliated unilamellar crystallites has attracted much interest since the delamination phenomenon of

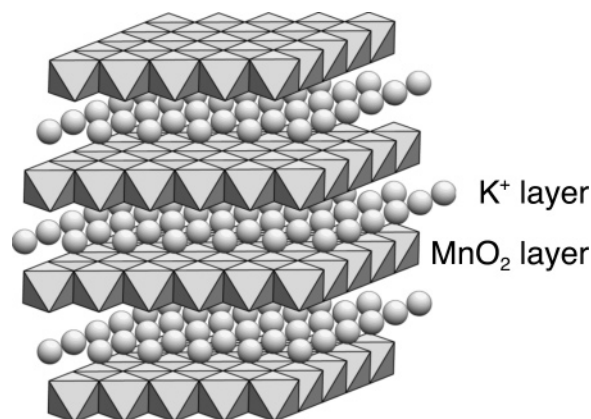


Figure 1. Crystal structure of α -NaFeO₂-type layered manganese oxide, K_{0.45}MnO₂.

clay minerals was first reported. However, their limited quantities often make the structure analysis itself difficult. The nanosheet structure can be described as a two-dimensional lattice having a periodic arrangement of constituent atoms parallel to the sheets. In principle, conventional diffraction techniques cannot be used to reveal quantitative structural information normal to the sheet because of the absence of periodicity in this direction. Understanding of the nanosheet structure in an individual and unilamellar state of exfoliated sheets, not in the restacked form, is crucial in order to utilize and control their physicochemical properties. Such a very low concentration system makes the structure analysis more difficult. To the best of our knowledge, structure analysis of individual and unilamellar nanosheets to obtain quantitative data of periodic and nonperiodic arrangements and compare the data with the structural data of parent materials has not been developed.

Transmission electron microscopy (TEM) has been mainly applied for observation and structure analysis of various

* Address correspondence to this author. E-mail: inakai@rs.kagu.tus.ac.jp. Fax: +81-3-3235-2214. E-mail: sasaki.takayoshi@nims.go.jp. Fax: +81-29-854-9061.

[†] National Institute for Materials Science.

[‡] Tokyo University of Science.

[§] High Energy Accelerator Research Organization.

nanosheets.^{3,8,16–18} Nanosheet samples such as Ti_{0.91}O₂¹⁷ and Ca₂Nb₃O₁₀¹⁸ usually showed electron diffraction patterns composed of sharp spots, reflecting their two-dimensional atomic arrangements. In contrast, there were only diffuse scattering rods along the sheet normal, indicating that there is no periodicity. With respect to the MnO₂ nanosheet, Yang et al.¹⁹ reported the structural characterizations using various characterization techniques including TEM, which confirmed that the basic hexagonal architecture was preserved upon exfoliation. Electron diffraction data are very useful to deduce the structure symmetry. However, they do not generally provide accurate structural parameters such as lattice constants as well as interatomic distances.

Synchrotron radiation (SR) X-ray in-plane diffraction, which enables the two-dimensional crystallinity of inorganic and organic materials on a flat substrate to be characterized directly and nondestructively, has made a remarkable contribution to material science.^{20–22} Since the total reflection arrangement can enhance the diffracted X-ray and reduce background noise, yielding excellent surface sensitivity, this technique has been extensively applied to low-concentration systems of light atoms, e.g., monolayer organic films, to reveal their overall packing arrangements.^{23,24} As a result, even in-plane diffraction measurement in the laboratory for a monolayer film of the titania nanosheet could resolve recognizable peaks, although a long measuring time was needed.²⁵ An energy tunable synchrotron source with high intensity and low divergence, which is beneficial for probing long scattering vectors, allows in-depth refinement of structural parameters. A combination of the total reflection and these capabilities of SR is believed to be advantageous to structure analysis of the monolayer of the MnO₂ nanosheets and precise structural parameters of two-dimensional unit cells can be obtained without damage through the measurements.

Another hurdle for structure analysis is to obtain nonperiodic structural information perpendicular to the sheet as aforementioned. This difficulty can be overcome with XAFS analysis, which can reveal the local structure of particular atoms even for noncrystalline or nanocrystalline materials. Recently, we have demonstrated that polarization-dependent fluorescence XAFS (PTRF-XAFS) under total external reflection is a powerful tool to reveal the three-dimensional framework of constituent atoms in the monolayer state of titania nanosheet crystallites.²⁶ Especially when the electric vector of X-rays is perpendicular to the sheet direction in the p-polarization arrangement, we can selectively probe the nonperiodic structure normal to the sheet.

In the present study, the structure of an individual and unilamellar state of MnO₂ nanosheets was revealed by the combined use of SR in-plane diffraction and PTRF-XAFS measurements. The obtained quantitative structural information clarifies the structural modification induced by the delamination.

Experimental Section

Material Synthesis. A manganese oxide of K_{0.45}MnO₂ with a rhombohedral layered structure²⁷ (Figure 1) was synthesized as a precursor of the nanosheets by calcination of a stoichiometric mixture of K₂CO₃ and Mn₂O₃ at 750 °C under oxygen atmosphere. The product was treated with a 1 mol dm⁻³ HCl solution for 10 days to be converted into an acid-exchanged form, H_{0.13}MnO₂·0.7H₂O.⁸ This acid-exchanged form (0.4 g) was vigorously shaken with a tetrabutylammonium hydroxide ((C₄H₉)₄NOH; TBAOH) solution (100 cm³, 5.2 × 10⁻³ mol) at ambient temperature for 10 days. A dark-brown suspension

was obtained and the unilamellar nanosheets with a composition of MnO₂ were separated from the unexfoliated material by centrifugation at 10 000 rpm for 30 min.

A monolayer film of the nanosheets was obtained by electrostatic self-assembly onto a substrate. Si wafers and quartz glass plates were used as an appropriate substrate for SR in-plane diffraction and PTRF-XAFS measurements, respectively. They were cleaned by immersing in HCl/CH₃OH (1:1) solution and then in concentrated H₂SO₄ solution. After being dipped into an aqueous solution of polyethylenimine (PEI, pH 9, 2.5 g dm⁻³) for 20 min to make the surface positively charged, they were immersed in a colloidal suspension of negatively charged manganese oxide nanosheets (pH 9, 0.08 g dm⁻³) for 20 min. An AFM image of the resultant film displayed a dense monolayer of the MnO₂ nanosheets with an average thickness of 8–9 Å.⁸ This value is larger than a crystallographic thickness of 5 Å, which may suggest some adsorbed species; one of the most likely species is H₃O⁺ for charge compensation. The monolayer films, in which the nanosheets lay flat to the substrate, were fabricated and were subjected to the following characterizations.

Synchrotron Radiation In-Plane Diffraction. In-plane diffraction measurements utilizing synchrotron radiation were performed at the Photon Factory BL-3A in the Institute of Materials Structure Science, High Energy Accelerator Research Organization (KEK-PF). An X-ray with a wavelength of 1.0895-(1) Å was obtained by using Si(111) double-crystal monochromators with a sagittal focusing optics. The X-ray beam was focused on the incident slit (0.05 × 10 mm²) by means of the sagittal focus system and two Pt mirrors coated on fused quartz. The incident angle was adjusted so that the sample surface was struck at an angle suitable for total reflection (0.14°). The in-plane diffraction pattern was measured by rotating the specimen and scanning the NaI scintillation counter fixed at the grazing exit angle (0.14°) around a horizontal plane of the film sample. The divergence of the diffracted beam along the in-plane direction was restricted by a soller slit (0.4°) placed in front of the detector. The details of the goniometer system, performance, and alignment were described in the literature.²⁸

Polarization-Dependent Total Reflection Fluorescence XAFS. XAFS measurements were carried out at BL-12C of the Photon Factory under total reflection fluorescence XAFS mode. Synchrotron radiation X-rays were monochromated by Si(111) double crystals and horizontally focused by a mirror. The beam size was adjusted by X–Y slits which provided a square flux of 0.2 × 2 mm² and 0.8 × 1 mm² for s- and p-polarization, respectively. The intensity of the incident X-rays (*I*₀) was monitored by an ionization chamber. The incident angle was adjusted by placing a sample plate on a Θ–Z stage below the critical angle (~0.30°) for the total reflection. The X-ray fluorescence intensity (*I*_f) generated from the nanosheet film was detected by a 19-element Ge solid-state detector arranged in a horizontal plane. Polarization-dependent measurements for the film sample were conducted by changing the geometrical configuration of the film with respect to the incident X-ray beam. An XAFS spectrum for a pellet sample of the protonic oxide H_{0.13}MnO₂·0.7H₂O was collected in a conventional transmission mode. All Mn K-edge XAFS spectra were measured at room temperature in an energy range from 6087 to 7637 eV with an interval of 1.0 and 2.5 eV for XANES and EXAFS regions, respectively.

Polarization-dependent total reflection fluorescence XAFS (PTRF-XAFS) spectra were calculated directly from the intensity ratio of *I*_f to *I*₀ without any correction for self-absorption because

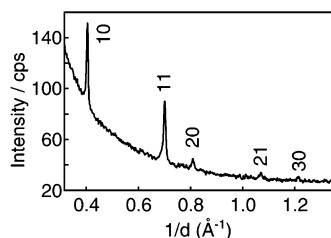


Figure 2. SR in-plane diffraction pattern for the monolayer of the MnO_2 nanosheets.

of the very small sample thickness. The EXAFS oscillations $\chi(k)$ (where k is the photoelectron momentum) were extracted from the measured spectra by using a spline-smoothing method performed with the EXAFS analysis program of RIGAKU REX2000 (version 2.3.2). The k^3 -weighted $\chi(k)$ was then Fourier transformed. The backscattering amplitude and phase function for each shell distance (Mn–O, Mn–Mn) in the curve-fitting analysis of the MnO_2 layer were estimated from feff8.00 calculation²⁹ of β - MnO_2 ,³⁰ which has atomic interactions similar to the present materials in terms of species and distance. The Debye–Waller factors were first set to 0.0036 \AA^2 and then optimized by the least-squares calculation considering the polarized coordination number. The goodness of fit was calculated as follows:

$$R_f = \frac{\sum \{k^3 \chi_{\text{obs}}(k) - k^3 \chi_{\text{cal}}(k)\}^2}{\sum \{k^3 \chi_{\text{obs}}(k)\}^2} \quad (1)$$

The error of each parameter was estimated from the square root of the diagonal element of the covariance matrix, which is recommended by IXS (The International XAFS Society).³¹

Results

In-Plane Diffraction of the MnO_2 Layer. The SR in-plane diffraction pattern for the monolayer film of the MnO_2 nanosheets was successfully obtained as shown in Figure 2. In the $1/d$ -region from 0.3 to 1.3 \AA^{-1} , five sharp reflections were detected. These peaks can be indexed in terms of a two-dimensional hexagonal cell, indicating that the exfoliated MnO_2 nanosheet retains its two-dimensional structural order similar to that of the starting material. A cell parameter, $a = 2.8565(4) \text{ \AA}$, was obtained with a high precision by the least-squares calculation. It is interesting to compare this value with that for the precursor protonated phase, $a = 2.842(8) \text{ \AA}$. The exfoliation brought about a 1% expansion of the sheet area. This expansion is likely to be dependent on the mean oxidation number of Mn, which will be discussed later.

EXAFS Analysis of $\text{H}_{0.13}\text{MnO}_2 \cdot 0.7\text{H}_2\text{O}$. The protonic manganese oxide $\text{H}_{0.13}\text{MnO}_2 \cdot 0.7\text{H}_2\text{O}$ did not have a regular layer-stacking, as revealed by a saw-tooth like profile for hk bands in the powder XRD pattern. This structural disorder makes it difficult to carry out the normal structure analysis, e.g., Rietveld refinement. Thus its structure was examined by EXAFS analysis. Figure 3 shows the Fourier transform (FT) of k^3 -weighted Mn K-edge EXAFS oscillation between $k = 2.45$ and 12 \AA^{-1} extracted from the XAFS spectrum of the protonic oxide. Two main FT peaks at 1.47 and 2.40 \AA are assigned to the Mn–O and Mn–Mn interactions, respectively, based on the coplanar host layer in the original material composed of edge-shared MnO_6 octahedra (see Figure 4). A starting model consisting of a first shell of Mn–O and a second shell of Mn–Mn gave a satisfactory fitting of the EXAFS pattern as shown by calculated and observed inverse Fourier transforms in the region of 1.0 – 2.8 \AA (Figure 5). The obtained structural

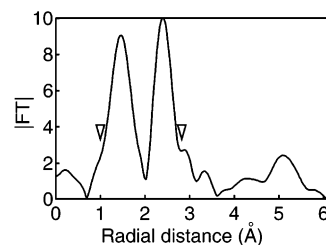


Figure 3. Fourier transforms of $k^3\chi(k)$ spectra in the weighting window of 2.45 – 12 \AA^{-1} for the protonic oxide of $\text{H}_{0.13}\text{MnO}_2 \cdot 0.7\text{H}_2\text{O}$. The triangles show the analyzed FT region from 1.0 to 2.8 \AA .

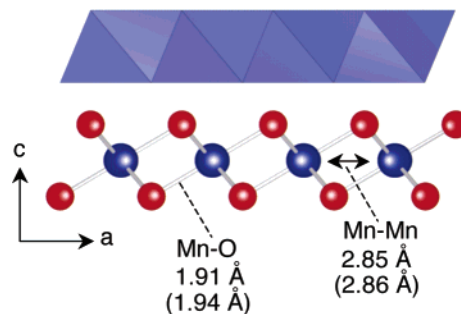


Figure 4. Structure illustration for the MnO_2 sheet projected onto the $[010]$ plane. Blue and red circles represent Mn and O atoms, respectively. The axis notation refers to the hexagonal symmetry of the host layer of bulk layered manganese oxide. Mn–Mn and Mn–O interatomic distances obtained from the present EXAFS analyses are shown as values with and without parentheses for the MnO_2 nanosheet and the protonic oxide of $\text{H}_{0.13}\text{MnO}_2 \cdot 0.7\text{H}_2\text{O}$, respectively.

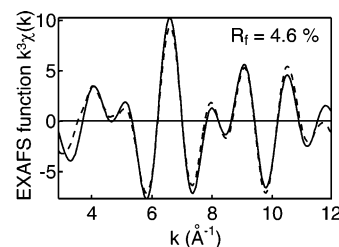


Figure 5. Inverse Fourier transforms of the radial distance from 1.0 to 2.8 \AA in the FT pattern of the protonic oxide of $\text{H}_{0.13}\text{MnO}_2 \cdot 0.7\text{H}_2\text{O}$. The solid line and broken line show experimental data and fitting pattern, respectively. R_f is defined by eq 1.

TABLE 1: EXAFS Parameters of $\text{H}_{0.13}\text{MnO}_2 \cdot 0.7\text{H}_2\text{O}$

interaction	N^a	$R \text{ (\AA)}^b$	$\sigma^2 \text{ (\AA}^2\text{)}$
Mn–O	[6]	1.91 ± 0.01	0.003 ± 0.001
Mn–Mn	[6]	2.85 ± 0.01	0.005 ± 0.001

^a N : coordination number. ^b R : interatomic distance.

parameters are listed in Table 1. The obtained Mn–Mn interatomic distance, $2.85 \pm 0.01 \text{ \AA}$, is in good agreement with the cell parameter of $2.842(8) \text{ \AA}$ refined from the XRD data.

Polarized EXAFS Analysis of MnO_2 Nanosheets. Thanks to the total external reflection of incoming X-ray, well-defined fluorescence XAFS spectra were successfully obtained both under two geometrical arrangements, s- and p-polarization, even from the monolayer film of the MnO_2 nanosheets despite its very low concentration ($0.7 \mu\text{g cm}^{-2}$). As can be seen in Figure 6a, Mn K-edge k^3 -weighted $\chi(k)$ for the MnO_2 nanosheets showed a marked dependence on the polarization vector. The polarization effect is much more manifest in the FT pattern of the $k^3\chi(k)$ (see Figure 6b). Two prominent peaks at 1.39 and 2.38 \AA were observed in the s-polarization data. It is found that there is a similarity between the s-polarization data and that of the protonic oxide in Figure 3. A slight difference in intensity

TABLE 2: EXAFS Parameters of the MnO₂ Nanosheets^a

interaction	$N^*{}^b$		R (Å) ^c		σ^2 (Å ²)
	p	s	p	s	
Mn–O	5.3 ± 0.3	6.6 ± 0.4	1.94 ± 0.01	[1.94]	0.002 ± 0.001
Mn–Mn		8.4 ± 0.5		2.86 ± 0.01	0.006 ± 0.001

^a p: p-polarization. s: s-polarization. ^b N^* : effective coordination number. ^c R : interatomic distance.

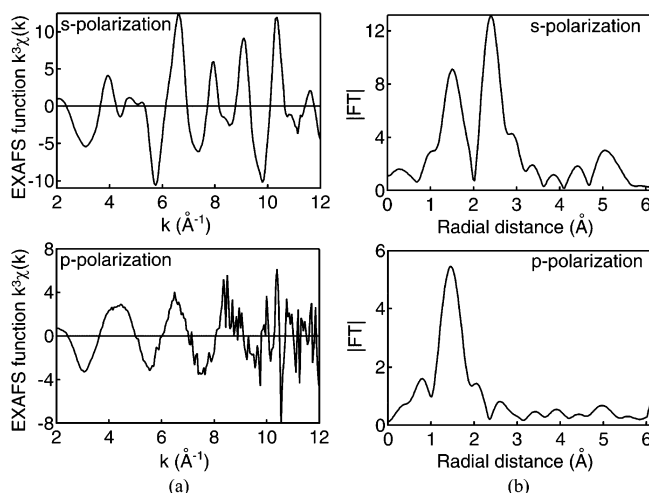


Figure 6. (a) Mn K-edge EXAFS spectra of the MnO₂ nanosheets from p- and s-polarization data which were extracted from raw data. (b) Fourier transforms of $k^3\chi(k)$ spectra in the weighting window of 2.45–10 Å⁻¹ for p-polarization data and 2.45–12 Å⁻¹ for s-polarization data.

ratio of the first and second peaks may be due to the polarization effect. This fact strongly suggests that the local structure of the MnO₂ sheets remains nearly unchanged after exfoliation into the single unilamellar crystallite. In contrast, the p-polarization data exhibited only one peak at 1.46 Å. This sharp contrast between s- and p-polarization can be understood by the structural aspect of this α-NaFeO₂-type sheet as shown in Figure 4. Since the Mn–Mn interactions yielding the peak at 2.38 Å in s-polarization are ideally perpendicular to the p-polarization vector, their contribution to the total EXAFS oscillation can be neglected. Consequently, Mn–O interactions in MnO₆ octahedra dominantly contribute to the p-polarized EXAFS oscillation.

On the basis of the above assignment, a single shell model involving Mn–O interaction and a double shell model with Mn–O and Mn–Mn interactions were used for the curve fittings of p- and s-polarized data, respectively. Note that the s-polarization data were analyzed by adding new parameters of Mn–Mn interaction to the parameters of Mn–O interaction obtained through the fitting of the p-polarization data. The best-fitted parameters are summarized in Table 2. Satisfactory fitting was attained, as demonstrated by inverse Fourier transforms of FT for p-polarization (1.0 Å < R < 1.9 Å) and s-polarization (1.0 Å < R < 2.8 Å) (see Figure 7). The obtained Mn–Mn distance of 2.86 Å for the MnO₂ nanosheets agrees well with the in-plane unit cell parameter of 2.8565(4) Å. When compared with the protonic oxide, the Mn–O distance of the nanosheets became significantly larger, while the Mn–Mn distance was nearly the same. Thus, the enlargement of the Mn–O interaction from 1.91 ± 0.01 to 1.94 ± 0.01 Å is significant, corresponding to a 1–2% expansion of the sheet thickness.

XANES Analysis of Manganese Ions in the MnO₂ Sheets. XANES spectra provide qualitative information on the average oxidation state of a target atom. Polarized Mn K-edge XANES spectra for the MnO₂ nanosheets are shown in Figure 8 together with the data for the protonic oxide. Both polarized spectra

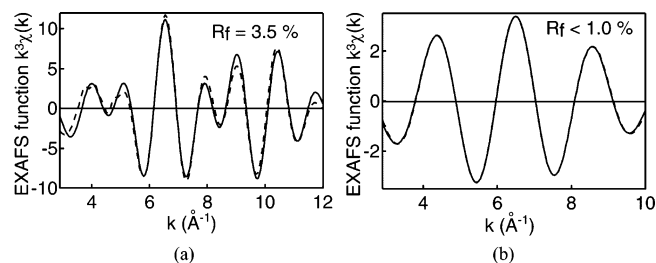


Figure 7. Inverse Fourier transforms of the radial distance from (a) 1.0 to 1.9 Å in p-polarization and (b) 1.0 to 2.8 Å in s-polarization FT patterns of the MnO₂ nanosheets. The solid line and broken line show experimental data and fitting pattern, respectively. R_f is defined by eq 1.

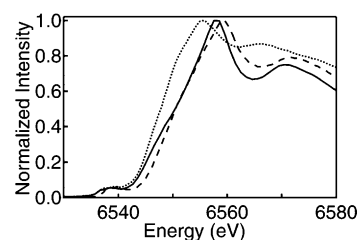


Figure 8. XANES spectra for H_{0.13}MnO₂·0.7H₂O (broken line) and the MnO₂ nanosheets under p- (dot line) and s-polarization (solid line).

exhibited a preedge feature that can be assigned to transitions from the core 1s level to unoccupied 3d states or hybridization states of 3d and 4p states in the MnO₆ octahedron.³² This preedge feature was followed by the white line peaks assignable to the dipole-allowed transitions from the core 1s level to the unoccupied 4p state of manganese. There is a large difference between p- and s-polarization spectra in terms of the energy and shape of the white line peak. The structural anisotropy of the MnO₂ nanosheet may account for this dependence on the polarization. A similar difference with respect to the polarization was observed for the XANES spectra of the titania nanosheet.²⁶

An XANES spectrum of the protonic oxide is located at higher energies than the data for the nanosheet in both s- and p-polarization. This energy shift may be ascribed to a higher average oxidation state of Mn ions having a larger attractive potential of the nucleus on the 1s core electron for the protonic oxide. This suggests that the mean oxidation state of Mn ions decreased upon exfoliation.

Discussion

The XAFS analyses in the present study have clarified the structural aspects of molecular MnO₂ nanosheets: the two-dimensional symmetry of the MnO₂ sheet, namely a hexagonal atomic architecture, was preserved even after exfoliation into the unilamellar nanosheet, while expansion of the sheet area (<1%) and the thickness (1–2%) was clearly revealed. These changes indicate that the volume of the MnO₆ octahedron increased to some extent upon delamination. This expansion should be associated with the decrease in mean oxidation number of manganese ions suggested by the XANES spectra for the MnO₂ sheets.

The oxidation number of the manganese ions in the MnO₂ sheets is numerically evaluated by Bond Valence Sum³³ (BVS), which can be regarded as an effective valence for the manganese ions, as calculated by:

$$\text{BVS} = \sum \exp\{(R_{\text{const}} - R_{\text{obs}})/0.37\} \quad (2)$$

where R_{const} is the bond valence parameter of 1.753 for the Mn⁴⁺ ion listed in the Brown's table.³³ R_{obs} is the Mn–O interatomic distance listed in Tables 1 and 2 for the protonic oxide and the MnO₂ nanosheet, respectively. BVS of the protonic material is 3.9 ± 0.1 , being in fairly good agreement with the result of chemical titration (3.87).⁸ On the other hand, the BVS for the MnO₂ nanosheet gives 3.6 ± 0.1 . These estimations are compatible with the interpretation of the energy shift of XANES spectra.

It is known that the K-type layered manganese oxide undergoes redox disproportionation as well as K⁺/H⁺ ion exchange via the acid treatment. As a result, the average oxidation number of the constituent manganese ions in the solid increased from 3.55 to 3.87.⁸ The oxidation brought about a contraction of the hexagonal packing of the host layer. On the contrary, the delamination into the MnO₂ nanosheet was accompanied by a reduction of the constituent manganese ions as mentioned above. The reduction may be promoted by the basic media of TBAOH solution used as a delaminating reagent. The potential of oxygen gas evolution generally becomes lower at higher pH. Although the quantitative information on the redox potential of Mn ions in the present system is not available, it is likely that the protonic oxide of H_{0.13}MnO₂·0.7H₂O oxidatively decomposes H₂O besides the delamination reaction. As a consequence, the manganese oxide itself is reduced. A similar reduction takes place in the synthetic process of a superconducting layered cobalt oxide from γ -Na_{0.7}CoO₂.³⁴ This reduction can account for the volume increase of the MnO₆ octahedron, which triggers the expansion of both the sheet area and the thickness. Yang et al.¹⁹ have reported that there was no appreciable change in the oxidation state of Mn ions during the exfoliation process on the basis of the data for starting K-type, protonated, and restacked samples. A similar result has been obtained in our previous study for restacked MnO₂ nanosheets with Li ions.¹² We assume that the nanosheets were oxidized again upon restacking.

It is of great interest to compare the structural modifications induced by exfoliation with those for another system of the titania nanosheet with a composition of Ti_{0.91}O₂.⁶ The exfoliation of the titania system Ti_{0.91}O₂ gave rise to ~2% shrinkage of sheet area (see Supporting Information I) and ~4% expansion of the sheet thickness²⁶ when compared with the precursor layered titanate of Cs_{0.7}Ti_{1.825}O₄. In the case of the titania nanosheet, the TiO₆ octahedra are combined with each other via edge-sharing in a zigzag fashion, which yields two planes of titanium atoms and four planes of oxygen atoms along the sheet normal. Once released from the crystalline layered structure, the thickness of the oxide sheet expands to relax electrostatic repulsion between the upper and the lower titanium ions facing each other. The shrinkage of the sheet area may be understood as a compensating action of the thickness expansion. In contrast, the MnO₂ nanosheet consists of only one plane of manganese atoms sandwiched by two planes of oxygen atoms (see Figure 4). This structure has no way to relax the repulsion between Mn ions by thickness expansion. Thus the sheet thickness is relatively insensitive to delamination. It is noteworthy that the magnitudes of the structural modification of the MnO₂ sheets were smaller than those for the titania

nanosheet. As described, they are reasonably explained by the changes of oxidation number of manganese ions. The large difference of structural modification between the two kinds of oxide nanosheets upon exfoliation emphasizes the importance of direct examination of both atomic arrangement and oxidation number of constituent atoms through structure analysis of the molecular state of exfoliated unilamellar crystallites. The present study indicated that a combination of SR in-plane diffraction and PTRF-XAFS promises to promote understanding of the structure of a wide variety of exfoliated unilamellar crystallites.

Conclusion

Both periodic and nonperiodic structural aspects of unilamellar MnO₂ nanosheets have been revealed by means of SR in-plane diffraction and PTRF-EXAFS analysis. The change in the oxidation state of constituent manganese ions in the nanosheet crystallites was deduced from XANES study, which was further supported by BVS calculation based on the resultant structural parameters obtained from EXAFS analysis. This study provides fundamental information on the structure of manganese oxide nanosheets in the molecular state, which will be useful for the understanding of their physical properties and industrial applications.

Acknowledgment. This work was financially supported by CREST of Japan Science and Technology Agency (JST). SR in-plane diffraction experiments and PTRF-XAFS were performed with the approval of the Photon Factory Program Advisory Committee (2003G271 and 2003G270, respectively). Figure 4 was drawn with VENUS developed by R. A. Dilanian and F. Izumi (National Institute for Materials Science).

Supporting Information Available: Figure S1 showing SR in-plane diffraction pattern for the monolayer of the titania nanosheets obtained via chemical delamination of lepidocrocite-related layered titanate. This material is available free of charge via the Internet at <http://pubs.acs.org>.

References and Notes

- (1) Walter, G. F. *Nature* **1960**, *187*, 312.
- (2) Nadeau, P. H.; Wilson, M. J.; McHardy, W. J.; Tait, J. M. *Science* **1984**, *225*, 923.
- (3) Leaf, A.; Schöllhorn, R. *Inorg. Chem.* **1977**, *16*, 2950.
- (4) Joensen, P.; Frindt, R. F.; Morrison, S. R. *Mater. Res. Bull.* **1986**, *21*, 457.
- (5) Treacy, M. M. J.; Rice, S. B.; Jacobson, A. J.; Lewandowski, J. T. *Chem. Mater.* **1990**, *2*, 279.
- (6) Sasaki, T.; Watanabe, M.; Hashizume, H.; Yamada, H.; Nakazawa, H. *J. Am. Chem. Soc.* **1996**, *118*, 8329.
- (7) Liu, Z.-H.; Ooi, K.; Kanoh, H.; Tang, W.-P.; Tomida, T. *Langmuir* **2000**, *16*, 4154.
- (8) Omomo, Y.; Sasaki, T.; Wang, L. Z.; Watanabe, M. *J. Am. Chem. Soc.* **2003**, *125*, 3568.
- (9) Armstrong, A. R.; Bruce, P. G. *Nature* **1996**, *381*, 499.
- (10) Tian, Z.-R.; Tong, W.; Wang, J.-Y.; Duan, N.-G.; Krishnan, V. V.; Suib, S. L. *Science* **1997**, *276*, 926.
- (11) Moritomo, Y.; Asamitsu, A.; Kuwahara, H.; Tokura, Y. *Nature* **1996**, *380*, 141.
- (12) Wang, L. Z.; Takada, K.; Kajiyama, A.; Onoda, M.; Michiue, Y.; Zhang, L. Q.; Watanabe, M.; Sasaki, T. *Chem. Mater.* **2003**, *15*, 4508.
- (13) Sakai, N.; Ebina, Y.; Takada, K.; Sasaki, T. *J. Electrochem. Soc.* **2005**, *152*, 384.
- (14) Liu, Z.-h.; Yang, X.; Makita, Y.; Ooi, K. *Chem. Mater.* **2002**, *14*, 4800.
- (15) Wang, L. Z.; Omomo, Y.; Sakai, N.; Fukuda, K.; Nakai, I.; Ebina, Y.; Takada, K.; Watanabe, M.; Sasaki, T. *Chem. Mater.* **2003**, *15*, 2873.
- (16) Kaschak, D. M.; Johnson, S. A.; Hooks, D. E.; Kim, H.-N.; Ward, M. D.; Mallouk, T. E. *J. Am. Chem. Soc.* **1998**, *120*, 10887.
- (17) Sasaki, T.; Ebina, Y.; Kitami, Y.; Watanabe, M.; Oikawa, T. *J. Phys. Chem. B* **2001**, *105*, 6116.
- (18) Ebina, Y.; Sasaki, T.; Watanabe, M. *Solid State Ionics* **2002**, *151*, 177.

- (19) Yang, X.; Makita, Y.; Liu, Z.-h.; Sakane, K.; Ooi, K. *Chem. Mater.* **2004**, *16*, 5581.
- (20) Bunk, O.; Zeysing, J. H.; Falkenberg, G.; Johnson, R. L.; Nielsen, M.; Nielsen, M. M.; Feidenhans'l, R. *Phys. Rev. Lett.* **1999**, *83*, 2226.
- (21) Aruta, C.; Ricci, F.; Balestrino, G.; Lavanga, S.; Medaglia, P. G.; Orgiani, P.; Tebano, A.; Zegenhagen, J. *Phys. Rev. B* **2002**, *65*, 195408.
- (22) Willmott, P. R.; Schlepütz, C. M.; Herger, R.; Patterson, B. D.; Hassdenteufel, K.; Steurer, W. *Phys. Rev. B* **2005**, *71*, 094203.
- (23) Rapaport, H.; Kjaer, K.; Jensen, T. R.; Leiserowitz, L.; Tirrell, D. A. *J. Am. Chem. Soc.* **2000**, *122*, 12523.
- (24) Edgar, R.; Huang, J. Y.; Popovitz-Biro, R.; Kjaer, K.; Bouwman, W. G.; Howes, P. B.; Als-Nielsen, J.; Shen, Y. R.; Lahav, M.; Leiserowitz, L. *J. Phys. Chem. B* **2000**, *104*, 6843.
- (25) Fukuda, K.; Sasaki, T.; Watanabe, M.; Nakai, I.; Inaba, K.; Omote, K. *Cryst. Growth Des.* **2003**, *3*, 281.
- (26) Fukuda, K.; Nakai, I.; Oishi, C.; Nomura, M.; Harada, M.; Ebina, Y.; Sasaki, T. *J. Phys. Chem. B* **2004**, *108*, 13088.
- (27) Delmas, C.; Fouassier, C. Z. *Anorg. Allg. Chem.* **1976**, *420*, 184.
- (28) Omote, K.; Harada, J. *Adv. X-ray Anal.* **2000**, *43*, 192.
- (29) Rehr, J. J.; Mustre de Leon, J.; Zabinsky, S. I.; Albers, R. C. *J. Am. Chem. Soc.* **1991**, *113*, 5135.
- (30) Bolzan, A. A.; Fong, C.; Kennedy, B. J.; Howard, C. J. *Aust. J. Chem.* **1993**, *46*, 939.
- (31) Error Reporting Recommendations: A Report of the Standards and Criteria Committee adopted by the IXS Standards and Criteria Committee, 2000.
- (32) Bridges, F.; Booth, C. H.; Anderson, M.; Kwei, G. H.; Neumeier, J. J.; Snyder, J.; Mitchell, J.; Gardner, J. S.; Brosha, E. *Phys. Rev. B* **2001**, *63*, 214405.
- (33) Brown, I. D.; Altermatt, D. *Acta Crystallogr. B* **1985**, *41*, 244.
- (34) Takada, K.; Fukuda, K.; Osada, M.; Nakai, I.; Izumi, F.; Ruben, A. D.; Kato, K.; Takata, M.; Sakurai, H.; Takayama-Muromachi, E.; Sasaki, T. *J. Mater. Chem.* **2004**, *14*, 1448.